Modeling and Simulation of DC Electric Rail Transit Systems With Wayside Energy Storage

Mahdiyeh Khodaparastan, Oindrilla Dutta, Mahmoud Saleh, *Student Member, IEEE*, and Ahmed A. Mohamed, *Senior Member, IEEE*

***Abstract*—Electric rail transit systems are large consumers of electricity, which face challenges related to improving their overall energy efficiency. Although various solutions have been proposed to achieve this target, it is not feasible to implement and test all of them. Since finding the solution that is most appropriate to a given system is typically a site-specific problem, an accurate, validated, and reliable simulation tool is crucial. In this paper, a simulation model for studying wayside energy storage systems in dc electric rail transit system is presented. The proposed model provides a reliable tool for analyzing the behavior of the transit system during intervals that span from a small fraction of time (milliseconds) up to 24 h. In order to validate the proposed simulation model, its results were compared with real measurements of a standard subway system.**

***Index Terms*—DC electric rail systems, energy storage systems, simulation tool, wayside connection.**

I. Introduction

ELECTRIC rail transit systems have been undergoing rapid development in order to meet the ever-increasing demand for efficient and fast public transportation. Peak demand reduction and increasing the system energy efficiency are important challenges for all the agencies, especially electric transit system that is an enormous consumer of electricity. Therefore, new technologies and equipment are increasingly proposed and designed to make transit systems more reliable and efficient.

Currently, most of the trains are equipped with motors that have regenerative braking capability. In this type of vehicles, during deceleration, the motors act as generators and produce electricity. This energy, termed as regenerative braking energy, can be injected into the third rail and used by other neighboring accelerating trains or other possible loads of the system. If there is no train/load on the system to absorb this energy, the voltage of the third rail will increase and protection devices will disconnect the train from the third rail and the rest of this energy will be dumped into onboard resistors [1], [2]. One important solution is capturing this energy by installing wayside energy storage systems (ESSs).

Various types of energy storage systems are available, such as batteries, supercapacitors and flywheels [3]–[5]. In order to select, design and size the ESS for a specific application, an in-depth knowledge of system performance, such as the power profile of trains, substation power loading, available regenerative braking energy, etc., are required. Computer simulation is a fundamental tool for engineers to investigate a proposed new design, or a major modification to an existing system, before its implementation. Therefore, a reliable and accurate simulation tool is required to model the DC electric rail systems for investigating the implementation of ESSs.

Simulation of electric rail systems has been studied since late 1970s and several simulation and modeling tools have been presented by both the industry and academia. There are software packages, such as: TrainOps developed by LTK [6], Sitras Sidytrac by Siemens [7], eTraX Rail Traction Power by ETAP [8], Train Operation Model (TOM) developed by Carnegie Melon University [9], OpenTrack and Open Power Net developed by ETH University [10], [11]and Vehicle Simulation Program (VSP) by Vrije University of Brussel [12].

Generally, the simulation procedure of electrified transportation systems is based on load flow calculations when trains are modeled with a current/voltage source [13], [14]. Most of the work that has been done on load flow analysis of electrified transportation systems divide system modeling into two parts: (1) vehicle movement model; and (2) electric network model [15]–[17]. Railway dynamics, equations describing single train motion and electric power supply load flow calculations are presented in [18]–[23].

Beside the classical model of the train, new approaches like energetic macroscopic representation (EMR) method is also used to model electric rail transit system [24], [25]. EMR is a graphical description tool that classifies the system into the basic inter-connected components, such as the source of energy, accumulation of energy, conversion of energy, distribution of energy and switching element [26].

Nowadays, most of the new trains are equipped with the regenerative braking system. To recuperate this energy, solutions such as energy storage and reversible substation are proposed.

Manuscript received March 24, 2018; revised September 28, 2018 and November 21, 2018; accepted January 4, 2019. Date of publication January 24, 2019; date of current version March 14, 2019. This work was supported in part by the New York State Energy Research and Development Authority, Consolidated Edison, and in part by New York City Transit. The review of this paper was coordinated by Prof. M. Preindl. *(Corresponding author: Mahdiyeh Khodaparastan.)*

M. Khodaparastan, O. Dutta, and M. Saleh are with the Smart Grid Laboratory, Department of Electrical Engineering, City University of New York, New York, NY 10031 USA (e-mail: m.khodaparastan@gmail.com; oindrilla270591@gmail.com; mahmoudsah@hotmail.com).

A. A. Mohamed is with the Smart Grid Laboratory, Department of Electrical Engineering, City University of New York, New York, NY 10031 USA, on leave from the Department of Electrical Engineering, Minia University, Minia, Egypt (e-mail: amohamed@ccny.cuny.edu).

Digital Object Identifier 10.1109/TVT.2019.2895026

In this regards, some research works have been done on modeling regenerative braking energy, energy storage systems and reversible substation modeling for application in rail transit systems [3], [27]–[36].

Among the research works which are being carried out in this field, only a few studies consider multi-train operation and/or the availability of regenerative braking energy and modeling wayside energy storage systems. In [37], multi-train simulation with onboard supercapacitors is presented. In [38], modeling of two trains running on the same line with both onboard and wayside supercapacitor ESS is presented. Simplified modeling of multi-train operation with both wayside and onboard supercapacitor is presented in [39]. In [40], a modified current injection power flow algorithm is used to model multi-train operation.

The main contribution of this paper is to provide a simulation tool to study regenerative braking energy recuperation in DC rail transit system, and to investigate the performance of different types of wayside energy storage technologies on utilizing regenerative braking energy. In the proposed simulation technique, multi-train operation and several types of ESS technologies are considered and simulated. Another advantage of the proposed simulation tool over the previous works is the detailed system modeling. In the previous studies, the dynamic behavior of system components is neglected; trains and ESSs are modeled with current sources and substations are modeled as a voltage source behind a diode rectifier. In order to verify the reliability of the proposed simulation tool, the results are validated versus real measurement from a subway system.

The rest of the paper is organized as follows, the power supply network modeling is presented in Section II. Section III presents vehicle modeling and simulation. Modeling of different types of ESS is demonstrated in Section IV. Simulation and validation results are presented in Section V. A case study is presented in Section VI and finally, the paper is concluded in Section VII.

II. Power Supply Substation Modeling

In DC electric rail transit systems, the power required by trains is provided by a power supply network including rail network and substations. Generally, substations consist of voltage transformers that step down the voltage and a unidirectional rectifier that converts electricity from AC to DC. In order to increase the reliability of the power supply, two sets, each consisting of a transformer and a rectifier, are connected in parallel. One of the transformers is connected as Y-Δ and the other one is connected as Δ-Δ in order to avoid phase shift. A capacitor bank is added at the output of transformers for fixing its output voltage. There are circuit breakers, insulation and other protection devices at both AC and DC sides to increase the safety.

Substations feed DC voltage to the overhead line or third rail (a rail next to the running rail) to supply the train power. The magnitude of DC voltage depends on the power demand and length of the third rail. Typical values are 600-750V. However, there are also available systems with 1500V and 3000V [18]. More information about DC power supply networks can be found in [41], [42].

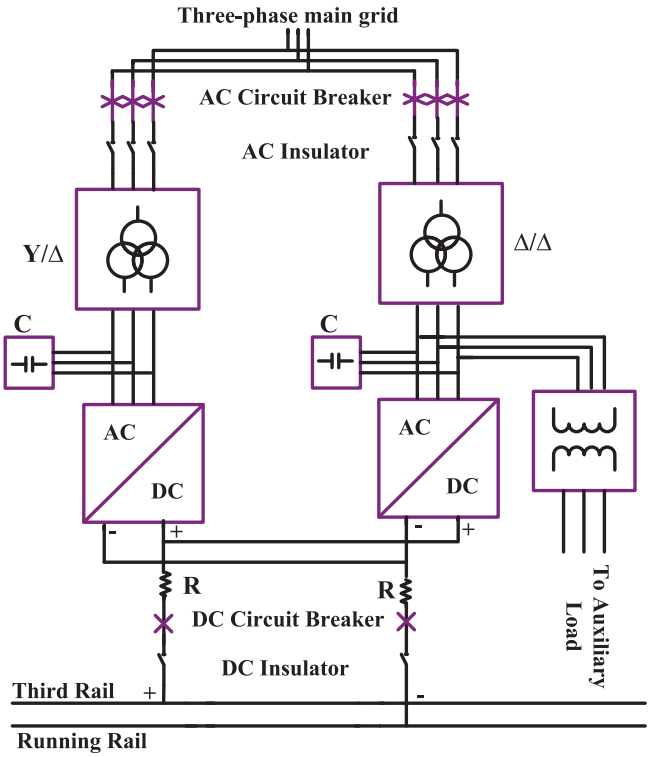

Fig. 1. Substation schematic.

TABLE I
Substation Parameters

Symbol	Description (unit)	Value
P_n	nominal power (kVA)	1663
f_n	nominal frequency (HZ)	60
V_1	RMS voltage of primary winding (V)	13200
V_2	RMS voltage of secondary winding (V)	465
R_1, R_2	resistance of primary and secondary winding (Ω)	2.66, 0.003
L_1, L_2	inductance of primary and secondary winding (μH)	6670, 9.19
R_m	magnetization resistance (Ω)	3000
L_m	magnetization inductance (Ω)	2000
C	capacitor bank (F)	0.001
R_{eq}	equivalent resistance	0.002

A detailed substation model that is used as a module in the proposed simulation tool is presented in Fig. 1. The description and values of the parameters related to each component are presented in Table I.

As mentioned above, vehicles get their required power from either overhead lines or third rails. Running rails provide a return path for the current and make the power circuit complete. The rail system network is divided into several sections to provide easy operation, protection and maintenance. Sections are connected to each other by means of traction circuit breakers. Depending on the status of circuit breakers, each section can be powered by one or two substations at both ends.

When a train moves on the traction rails, the resistances between the train and its departure and arrival points are changing based on the distance between them at each time instant [43].

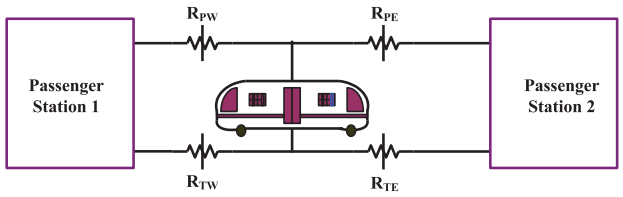

Fig. 2. Schematic of the train running between two passenger stations.

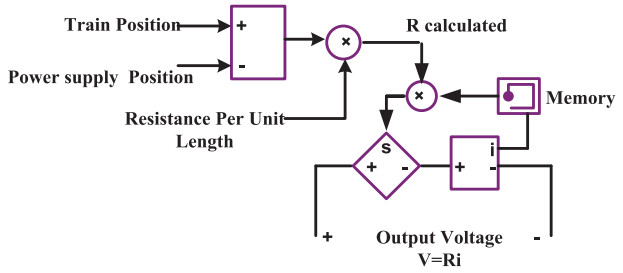

Fig. 3. Schematic of the variable resistance modeling.

In order to simulate the movement of vehicles, rail sections are modeled by variable resistances. Variable resistances are modeled by a controlled voltage source, as presented in Fig. 2. A section of the rail with a vehicle running from west to east is presented in Fig. 3. Equations related to each variable resistance are presented in (1) to (4) [43].

$$R_{PW} = x_p R_{power\_rail} \tag{1}$$

$$R_{PE} = (L - x_p) R_{power\_rail} \tag{2}$$

$$R_{TW} = x_p R_{traction\_rail} \tag{3}$$

$$R_{TE} = (L - x_p) R_{traction\_rail} \tag{4}$$

Where R_{PW} and R_{PE} are the power rail resistances at west and east side of the train. Similarly, R_{TW} and R_{TE} are the traction rail (running rail) resistances. R_{power_rail} and $R_{traction\_rail}$ are the resistances of power and traction rail per unit of length. L is the distance between two passenger station and x_p is the train position.

III. Train Modeling

There are two main approaches to model a train:

1) Forward modeling, known as cause-effect modeling.
2) Backward modeling, known as effect-cause modeling.

In forward modeling of the vehicle, the input (cause) will be current/power absorbed by the vehicle. By following the dynamics of every component of the vehicle, the speed of the wheels (effect) can be calculated. In backward modeling, the analysis is performed in the reverse direction, i.e., the speed of the wheels (effect) is considered as an input and, going backward through the various components, the current/power required by the vehicle (cause) is calculated.

In this study, the backward methodology is used to model the vehicles. The modeling process is presented in Fig. 4.

As illustrated, there are three main stages to calculate the required power of the train in the backward approach; including

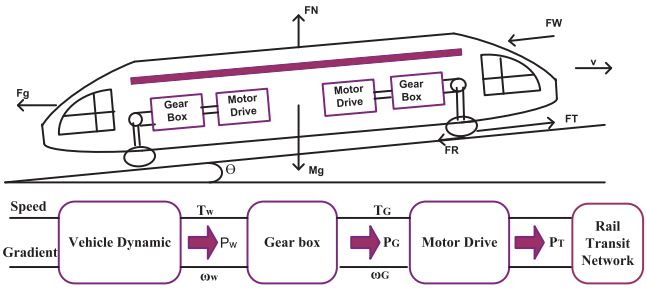

Fig. 4. Vehicle modeling process.

vehicle dynamic calculation stage, gearbox stages and motor's drive stages.

There are several forces applied to the wheels, including friction force (F_R), the force due to the wind (F_W) and gravity force (F_g). These forces should be overcome by the tractive effort (F_T) created by the motors of the vehicle. In the first stage, speed of the wheel (v) and inclination angle of the path (θ) are considered as inputs and using vehicle dynamic equations, (5) to (10), the tractive effort applied to the wheel is calculated and from there the required torque (T_w) and angular speed (ω_w) of the wheels are determined and used as inputs for the next stage, which is a gearbox. The role of a gearbox is to reduce the speed of the motor drive connected to its shaft while increase output torque of the motor drive. In the backward approach, using the equations that described the gearbox performance, (11) to (14), the required torque (T_G) and the speed of the motor drive (ω_G) are determined.

$$F_T - F_R - F_g - F_W = M_{Metro} \frac{dv}{dt} \tag{5}$$

$$F_R = f_R M_{Metro} g \cos\theta \tag{6}$$

$$F_g = M_{Metro} g \sin\theta \tag{7}$$

$$F_W = \frac{1}{2} C_w A \rho v^2 \tag{8}$$

$$T_w = \frac{F_T \times r}{4 n_{cars}} \tag{9}$$

$$\omega_w = \frac{v}{r} \tag{10}$$

Where, M_{metro} is the weight of the train, f_R is the friction factor, g is the acceleration gravity, C_w, A and ρ are drag coefficient, front area of the train and air density, respectively. The number of cars and the radius of the wheels are presented by n and r, respectively.

Gearbox equations in motoring condition are:

$$T_G = \frac{T_w}{\gamma_G} + \frac{B}{\gamma_G} \tag{11}$$

$$\omega_G = \omega_w \gamma_G \tag{12}$$

Where, γ_G is the gearbox ratio and B represents the vehicle losses and is calculated using (9).

$$B = T_w (1 - \eta_G) \tag{13}$$

Where, η_G is the gearbox efficiency.

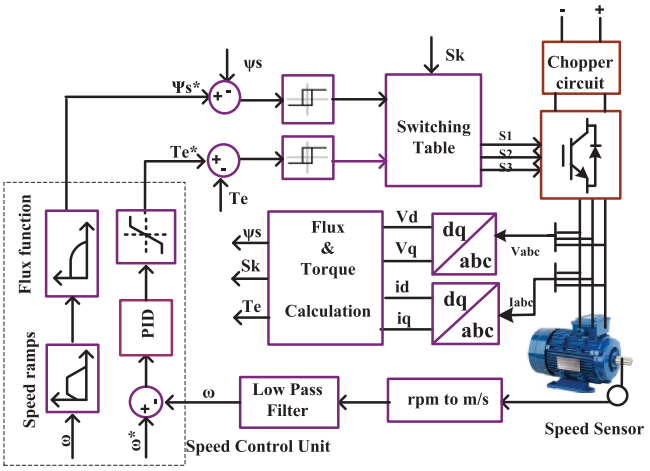

Fig. 5. Vehicle modeling process.

For the braking process (negative torque), (11) can be modified as follows:

$$T_G = \frac{T_w}{\gamma_G} - \frac{B}{\gamma_G} \tag{14}$$

In the last stage, the calculated torque and speed from the gearbox are given to the motor drive to calculate the current required by the vehicle.

In this paper, two models are proposed for drive modeling: 1) Detailed model and 2) Approximate model. In detailed modeling, every component of the vehicle's drive is represented and modeled, which makes the model more accurate but more complex and it takes the longer time to simulate. The Approximate model is less accurate but fast because it does not consider the dynamic behavior of every component.

A. *Detailed Modeling*

Electric trains consist of several cars connected to each other. Each car has a set of motor drive and gearboxes connected to a shaft. Each shaft has two wheels connected to it. Typically, a motor drive consists of the induction motors, an inverter and its controller, and a chopper circuit. To model the electric motor drive, a direct torque control (DTC)DTC drive available for AC machines in MATLAB/Simulink library has been modified and adopted. A schematic of the motor drive is presented in Fig. 5.

Control methods available for induction motor can be classified into two main groups: 1) scalar-based controller (control magnitude and frequency of variables in steady states); 2) vector-based control (control magnitude, frequency and the instantaneous position of space vector of the variable). Vector-based control also classified into filed oriented, feedback linearization, direct torque control and passively based control [44].

DTC control is used in this study to control the induction motor. This controller works based on control of stator voltage (output voltage of inverter). In this control strategy, at each time step, a voltage vector is applied to the inverter in order to reduce the error of torque and flux. There is no intermediate current

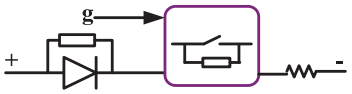

Fig. 6. Block diagram of the braking chopper.

controller in this technique which makes the controller fast and robust [45].

Most of the equations and description related to DTC controller is presented in the Appendix A. In summary, as illustrated in Fig. 5, the torque and flux are calculated from the voltage and current of the motor. Then the estimated torque and flux are compared with their references produced by the speed controller section. In the speed controller part, the speed of the motor, which is converted to m/s from rpm, is compared with the reference speed and the error is applied to the PID controller, followed by a limiter block. The limits depend on the motor rating. The output of this part is a reference torque. Flux reference is also produced from motor speed and flux calculation block worked based on (15) [44].

$$\psi_s = \sqrt{\left(\frac{L_s}{L_M}\psi_r\right)^2 + (\sigma L_s)^2\left(\frac{L_r}{L_M}\frac{T}{\psi_r}\right)^2} \tag{15}$$

Where, $\sigma = 1 - (M^2/L_s\,L_r)$.

The error of the torque and the flux are given to the hysteresis comparator, where the flux comparator has two limits based on the following conditions:

$$H_\psi = 1 \quad \text{for} \quad e_\psi > +HB\psi$$
$$H_\psi = -1 \quad \text{for} \quad e_\psi < -HB\psi$$

Where, e_ψ is the flux error and $\pm HB_\psi$ are the upper and lower hysteresis band of the flux. Torque hysteresis comparator has three limits based on the following conditions:

$$H_T = 1 \quad \text{for} \quad e_T > +HB_T$$
$$H_T = -1 \quad \text{for} \quad e_T < -HB_T$$
$$H_T = 0 \quad \text{for} \quad -HB_T < e_T < +HB_T$$

Where, e_{T} is the flux error and $\pm HB_T$ are the upper and lower hysteresis band of the torque. The flux hysteresis band has an impact on stator current distortion and torque hysteresis band affect the switching frequency [46]. The hysteresis controllers outputs along with sector index (θ_e) are used as inputs to the switching lookup table, presented in Table VI of Appendix A [47].

The last component in the motor drive is the breaking chopper. It consists of a resistor bank and an IGBT switch, which is controlled by a hysteresis controller. A schematic view of the braking chopper is presented in Fig. 6. The chopper circuit monitors the DC bus voltage, if the voltage goes above a prespecified value (upper limit activation voltage), the IGBT switch turns on. Then, the excess power on the line will be dissipated in the resistor bank. The switch is turned off when the voltage drops to the lower voltage limit (lower limit shut down voltage).

B. Approximate Model

Another approach that has been used for train modeling simplifies the system by modeling each component with a gain factor representing its efficiency.

The process of calculating torque and speed is similar to the detailed model. Using equations (5) to (10), the torque and speed applied to the motor drive are calculated. Then, the amount of power applied to the motor drive is calculated using equation (16).

$$P_d = T_w \times \omega_w \tag{16}$$

Having the efficiency of the gearbox, motor and inverter, the amount of power and current requested from the main grid is calculated by (17) and (18):

$$P_t = 4n_{cars}\left(\frac{P_d}{\eta_{gear}\eta_{motor}\eta_{inv}}\right) \tag{17}$$

$$I_t = \frac{P_t}{V_t} \tag{18}$$

In summary, given the speed profile and using equations (5) to (10) and (16) to (18), the electric vehicle can be modeled as a current controlled source that is connected to the rail system.

IV. Energy Storage Modeling

Batteries, supercapacitors and flywheels are three types of technologies commonly used in DC electric rail transit systems. In the MATLAB/Simulink environment, there are available models for battery and supercapacitor. These two options are modified and adopted based on the desired design and parameters. To connect the battery and supercapacitor to the electric rail system, a bidirectional DC/DC converter is designed and modeled. The Flywheel energy storage system is modeled using a permanent magnet machine connected to a rotating mass.

The detailed modeling description related to each type of ESS is presented in this section.

A. Batteries

The battery is modeled with a controlled voltage source in series with a resistance. This model is a generic dynamic model and can represent the different types of rechargeable battery, such as Lead-Acid, Lithium-Ion, Nickel- Cadmium and Nickel-Metal-Hydride. Each technology can be modeled by adjusting its parameters and equations. Fig. 7 presents a schematic view of the battery model. For the sake of brevity, the equations related to battery model is presented in Appendix B.

The battery is connected to the system by means of the bidirectional DC/DC converter, presented in Fig. 8.

During charging, only S_1 is turned on and during discharging mode only S_2 is turned on. More information about this type of bidirectional DC/DC converter can be found in [48]. The current (*I_command*) is produced by battery energy management unit that is working based on some general rules as follows:

1) If $V_{PCC} > V_{set\_ch}$, charging command up to a level of $SOC = 90\%$

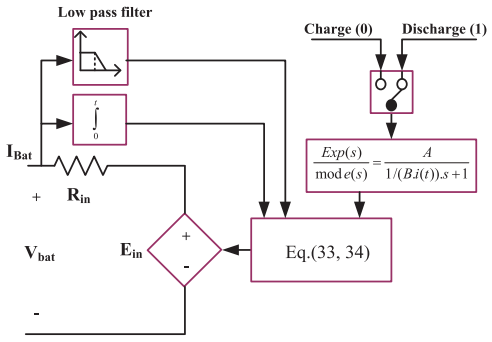

Fig. 7. Battery model.

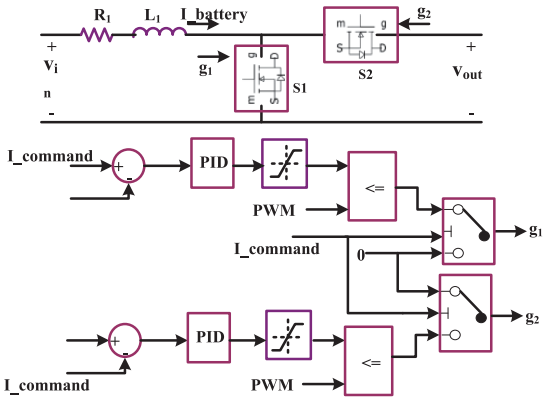

Fig. 8. Bidirectional DC/DC converter.

TABLE II
DC/DC Converter Parameter

Symbol	Description (unit)	Value
V_{in}	Battery output voltage (V)	645
V_{out}	Substation voltage (V)	500
D	Duty cycle	0.44
f	Switching frequency (kHz)	5
L_l	Input inductance (mH)	≥ 0.1
R_l	Inductance resistance (Ω)	3.2468

2) If $V_{PCC} < V_{set\_dis}$, discharging command up to a level of SOC = 40%
3) If $V_{set\_dis} < V_{PCC} < V_{set\_ch}$, no charge or discharge takes place.

Where V_{PCC} is the voltage of the line at the point of connection of the ESS, V_{set_ch} and V_{set_dis} are voltage levels that are set for triggering charging and discharging process, respectively. These voltage set values and charge/discharge current amplitudes depend on the application and goal of installing the ESS.

Parameters related to the DC/DC converter is presented in Table II.

B. Supercapacitors

Similar to the battery, a supercapacitor is modeled with a controlled voltage source in series with a resistor, as presented in Fig. 9.

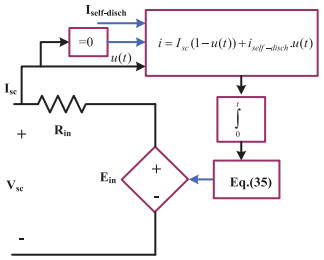

Fig. 9. Supercapacitor model.

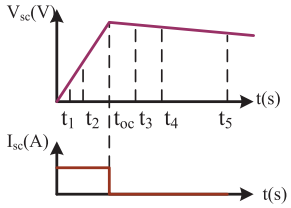

Fig. 10. Discharging current and voltage of supercapacitor.

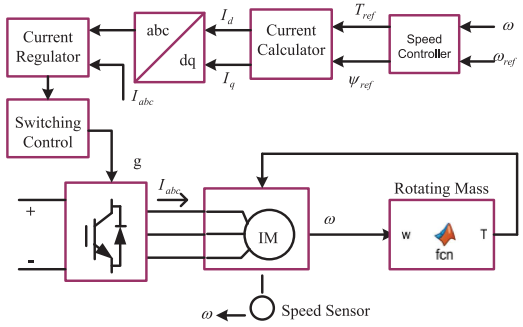

Fig. 11. Flywheel model.

As it is illustrated, if $i_{SC} = 0$, self-discharge current is considered for the supercapacitor which affects the electric charge ($Q(t)$). Self-discharge current is defined based on (19) and Fig. 10 that shows the self-discharge phenomena of supercapacitor.

$$i_{self-dis} = \begin{cases} \frac{C_t \alpha_1}{1+sR_{SC}C_T} & \text{if } t - t_{oc} \leq t_3 \\ \frac{C_t \alpha_2}{1+sR_{SC}C_T} & \text{if } t_3 < t - t_{oc} \leq t_4 \\ \frac{C_t \alpha_3}{1+sR_{SC}C_T} & \text{if } t - t_{oc} > t_4 \end{cases} \quad (19)$$

Where, C_T is the total capacitance, R_{SC} is the internal resistance and α_1, α_2 and α_3 are constants and are equal to the rate of change of supercapacitor voltage at the corresponding time interval.

Supercapacitor output voltage

C. Flywheels

A flywheel ESS consists of a rotating mass, an electric machine, which can act as a generator or motor, and power electronic interface. Schematic of flywheel modeling is presented in Fig. 11.

The rotating mass is modeled based on the flywheel's energy and speed equations and limitations. Since the rotating mass is coupled with the electric machine, its speed is equal to the speed of the machine. This speed is considered as an input to the rotating mass model. The speed of flywheel is limited between $\omega_{\min}$ and $\omega_{\max}$, which are the minimum and maximum speed allowed for flywheel operation, respectively. If the input speed is beyond the speed limit of flywheel, this speed will change to the boundary value. Then the energy of the flywheel is calculated based on (20).

TABLE III
FLYWHEEL PARAMETERS

Symbol	Description (unit)	Value
kWh_d	Delivered Energy (kWh)	0.52
P_{peak}	Peak (continuous) Power (kW)	375-750
M_s	System Mass (kg)	1000
ω_{max}	Flywheel maximum speed (rpm)	20000
ω_{min}	Flywheel minimum speed (rpm)	10000
V	Voltage (V)	420-800
I_{max}	Maximum current of each module (A)	167
K_p, K_i	Proportional and integral gain of speed controller	5, 100
T_{max}, T_{min}	Speed controller output torque saturation (N.m)	$\pm$ 256

$$E = \frac{1}{2} J\omega^2 \quad (20)$$

Where, E is the energy, J is the flywheel Inertia and ω is the flywheel speed. The flywheel power is presented by (21):

$$P = \frac{dE}{dt} \quad (21)$$

Having the power and speed of a flywheel, the mechanical torque input for the electric machine is calculated based on (22).

$$T = \frac{P}{\omega} \quad (22)$$

The electric machine used in this study is a permanent magnet synchronous machine, which is controlled via a 3-level AC/DC converter. During the charging process, the converter acts as an inverter and the electric machine acts as a motor and speeds up the flywheel. During the discharging process, the flywheel slows down and the motor acts as a generator, while the power electronic converter acts as a rectifier that injects the released energy of the flywheel to the third rail. The parameters and their values used for flywheel modeling are presented in Table III.

V. VALIDATION RESULTS

In order to validate our proposed simulation tool, a portion of line 7 of NYCT consisting of 3 substation and 4 passenger stations is considered as a case study. The schematic of this system is presented in Fig. 13. This system is simulated for several cases and the results are compared with real measurements. Firstly, the results are compared for one cycle operation and then they are compared for 24 hours operation.

A. One-Cycle Operation

In this section, several speed profiles from the real measurement are given to the train model and the output results, i.e., Third rail voltage and current of the trains, are compared with

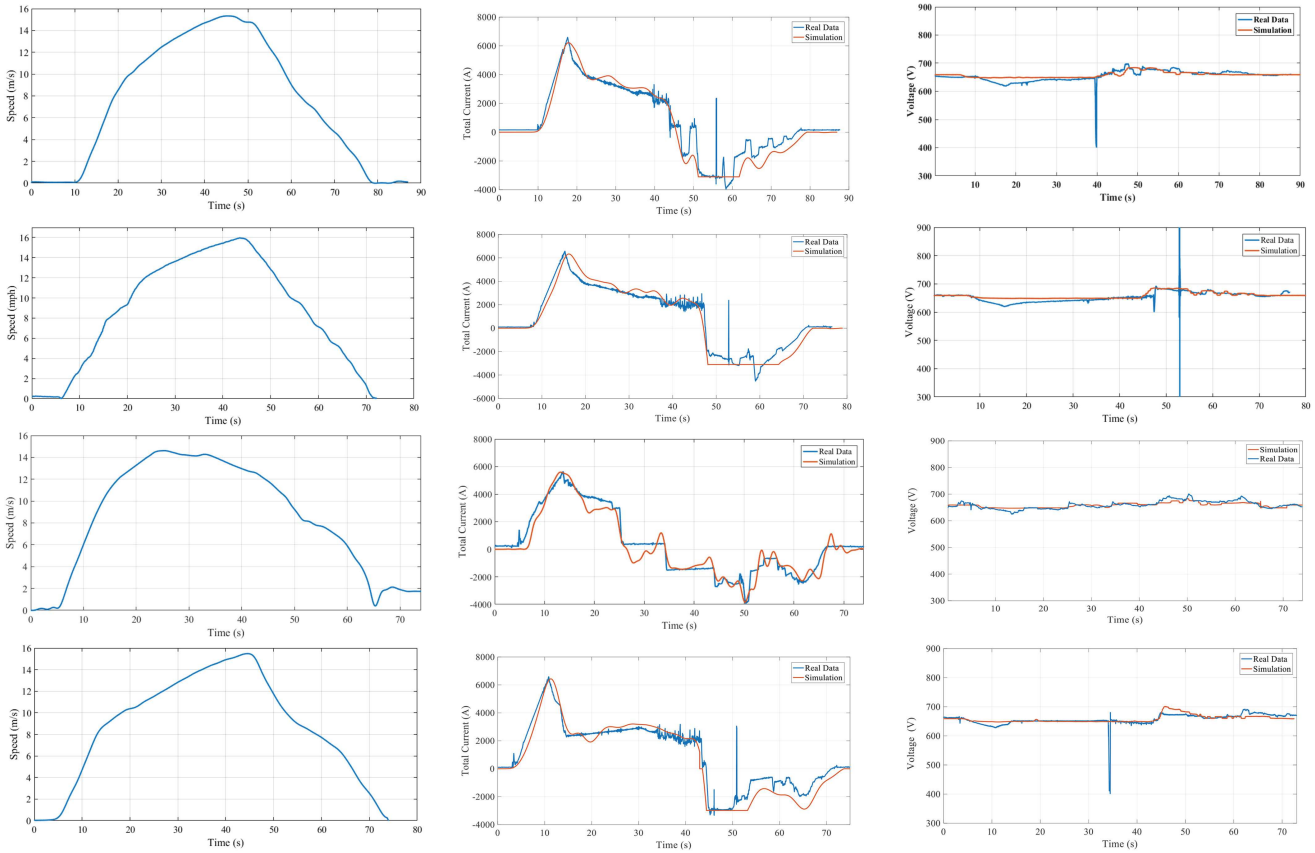

Fig. 12. Validation results for one-cycle operation.

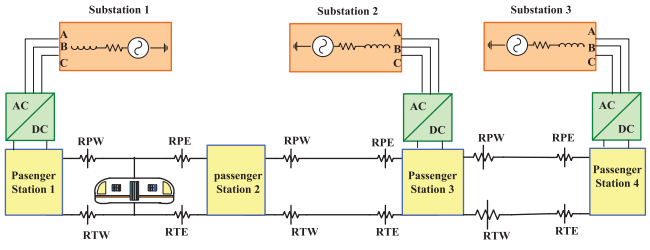

Fig. 13. Under study portion of electric rail transit system.

real measurements (5000 sample/second). Speed profiles which are given to the train as an input and related current and voltage are presented in Fig. 12. As illustrated, in the first 15-20s, the speed increases with the maximum acceleration and consequently the current rises to its maximum. During the same time interval, the voltage slightly decreases to a lower value. After this, the speed increases with a smaller acceleration rate until it reaches the maximum speed and the current gradually decreases to an almost constant value.

During deceleration, motors act as generators and produce electric current (the current is in reverse direction and here it is shown with negative values). The current will have different amplitude and shape, Based on the deceleration rate. In the last 20 seconds of deceleration, several fluctuations happen in the speed profiles which are reflected with larger fluctuations on the current.

The results from simulation versus real measurements show that, with each of the speed profiles, the current and the voltage from simulation closely follow the real measurements for current and voltage.

B. 24 Hours Operation

The single cycle operation of the rail transit model has been extended to a 24 hours operation for a more conclusive validation of the results. Besides, a 24 hours operation is imperative for the study of peak demand reduction of substations. This prototype has been obtained on the basis of train scheduling by NYCT [49]. The schedule provides information such as, headway between trains during different times of the day and the probability of two trains exchanging regenerative energy during peak hours of the day. This data is used to obtain factors for every fifteen minutes interval of the day, which when multiplied with the power and energy profiles of a single train can provide the energy consumption during every 15 minutes of 24 hours (as real data sampled). Two examples of 24 hours power profile of substation 1 and 2 in the system under study are illustrated in Fig. 14.

As it is illustrated, the power demand reduces gradually at night and then starts to increase in the early morning. There is a local maximum around 8:30 AM when the express and local trains run together and the time interval between trains is reduced to provide a fast and reliable service for a large number of passengers who are using transit system for commutation. After this time, as it is expected the headway between running trains increases and express train service stops. Therefore, power

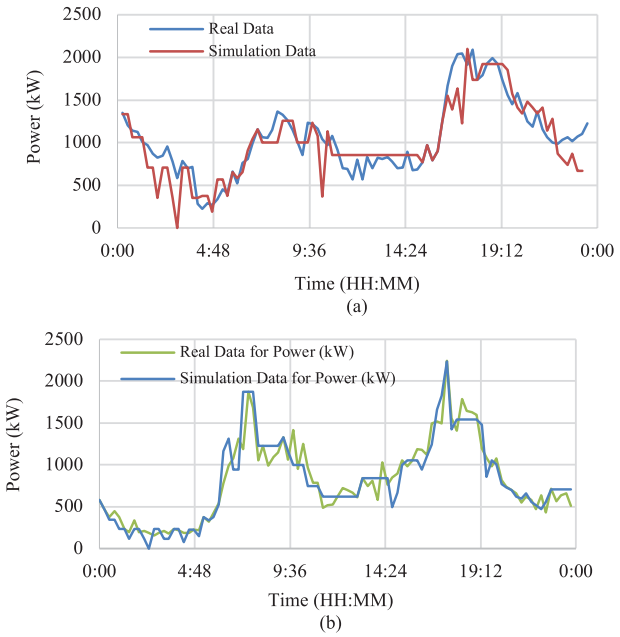

Fig. 14. 24 hours power profile of the substation1 (a) and the substation 2 (b) in system under study.

demand decreases and remains at an almost constant value until 3 PM in the afternoon, when the express service starts again. Also, the headway between running train decreases again and power demand increases until it reaches its maximum around 6:30 PM. In this time, the power demand of the substations goes beyond 2 MW.

Based on the approach explained earlier in this section, the 24 hours power profile of two substations are created and compared with real data. Those follow the same trend as real data and most of the time those are matched with each other. However, there are some points where they deviate from each other. This is due to the fact that the number of passengers on the trains may differ day by day, which affects the power drawn by the trains. Additionally, there may be a delay in the running time of some of the trains, so it affects the amount of power drawn from the substation in some 15 minutes interval. For example, if some delays happen and as a result of two trains, running in reverse direction, accelerate at the same time, twice the power of a single train is requested from the substation, which increases the demand during that interval.

VI. Case Study

In this section, the proposed model is used as a tool to test the impact of installation of three different technologies, including a battery, a supercapacitor and a flywheel, on peak demand reduction. A portion of the system presented in Fig. 13, is selected as a case study. ESSs will be installed at substation 2.

Fig. 15 presents the speed, current and power and energy profile of a train approaching substation 2. The change of total energy during acceleration (0 s-30 s) is about 14 kWh and the change of total energy during deceleration (30 s-63 s) is about 5kWh. In other words, almost 35% of the energy consumed during acceleration is available for energy recuperation. This energy can be saved into the ESS and released during train acceleration and consequently reduced the power and energy demanded from power supply substation [50]. In addition, it can improve the third rail voltage drop during train acceleration. Fig. 16 shows the current profile of the train, substation 2 current with and without ESS and charge/discharge current of ESS. The train current magnitude is higher than the substation 2 current because the other substations also contribute to supplying this current. When ESS installed in the substation as it is expected the current magnitude of the substation is reduced and consequently the power demanded from it will be reduced. During deceleration (30-63 s) ESS can be charged from regenerative braking energy produced by the train. Fig. 17. present

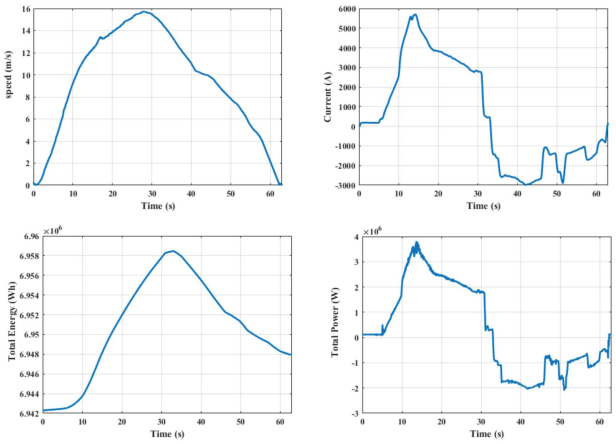

Fig. 15. Train, substation, and ESS current profiles.

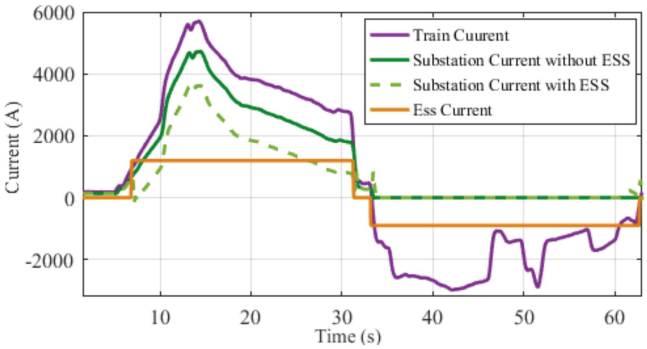

Fig. 16. Application of ESS on reducing peak current demand.

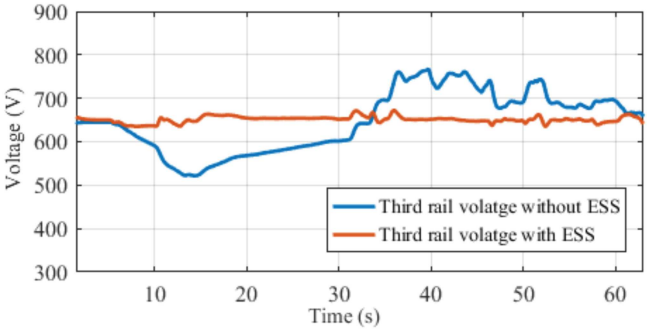

Fig. 17. Third rail voltage with and without ESS.

TABLE IV
ESS COMPARISON

Technology	Size	Cost ($)
Battery	1111.6 kWh , 570 kW	1333.914-50002.180
Supercapacitor	1.5 kWh, 570 kW	57750-250500
Flywheel	3.5 kWh, 570 kW	93100-247000

the voltage of the third rail with and without ESS. During acceleration since the train consumes high current magnitude in a short period of time, the voltage of the third rail is dropped suddenly to some lower voltage value (in extreme cases it can cause a damage to the train and other equipment connected to the third rail). Under voltage relay setting was set on 480 VDC in our case study and nominal voltage is 650 VDC. During train deceleration, regenerative braking energy is injected to the third rail and raise its voltage (here over voltage protection setting was set to 780 VDC). By installing ESS, this energy is used for charging ESS and voltage will be more stable.

To compare the performance of different technologies on peak demand reduction of substation 2; battery (Li-ion), supercapacitor and flywheel are sized for 10% peak demand reduction. The sizing information is presented in Table IV. The results show that to achieve a 10% peak demand reduction, battery needs to be oversized to be able to deliver required power during train acceleration (30 s). The cost comparison for each technology is also presented in Table IV. Battery has the highest installation cost and supercapacitor is the cheapest one. However, supercapacitor need to be replaced every 5 years [28], therefore the total cost of the supercapacitor for 10 years is higher than the flywheel.

VII. CONCLUSION

In this paper, a detailed simulation model for modeling DC electric rail system is presented. DC electric rail system consists of substations, rail systems, trains and energy storage systems.

Backward modeling approach is used to model the vehicle. In other words, by having the speed profile of the vehicle, current, power and the energy of the vehicle can be calculated. Different types of ESS technologies including batteries, supercapacitors and flywheels are described and modeled. The simulation results are compared with real measurements for one cycle and 24 hours operation. Comparison results showed the validity and accuracy of the proposed simulation tool. The proposed simulation technique can be used as a reliable tool for investigating the train performance in different case study, such as regenerative braking recuperation, potential application of ESS for peak demand reduction and energy saving in DC electric rail systems.

APPENDIX A

The torque and the flux of induction motor are related to each other based on (23):

$$T = \frac{3}{2}p\frac{L_M}{L_s L_r - L_M^2}\psi_r \psi_s \sin\delta_\psi \tag{23}$$

Where, L_M, L_r and L_s are the magnetizing, rotor and stator inductances, respectively. ψ_r and ψs are rotor and stator flux, and δ_ψ is the torque angle.

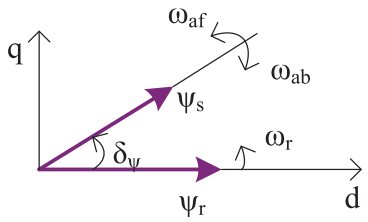

Fig. 18. Stator and rotor flux rotation.

Stator and rotor flux rotate with a linear speed in an approximately a circular path. A vector diagram of stator and rotor flux movement is presented in Fig. 18. In constant magnitude flux, if the speed of stator flux increases, the angle δ_ψ is increased and the torque value will reduce and if the speed of stator flux decreases or goes to zero, the angle δ_ψ is decreased and the torque will increase.

On the other hand, the stator flux is a state variable that can be controlled by the stator voltage based on (24).

$$V_s = V_{inv(n)} = 2\pi f\frac{d\psi_s}{dt} \tag{24}$$

Inverter output voltage space vector $V_{inv\,(n)}$ can be described with (25) and (26).

$$V_{inv(n)} = \begin{cases} (\frac{2}{3})v_{dc}e^{j(n-1)\pi/3} & n = 1,2,3,4,5,6 \\ 0 & 0,7 \end{cases} \tag{25}$$

$$v_{dc} = \frac{V_{dc}/\sqrt{2}}{V_{srated}} \tag{26}$$

Where, V_{srated} is the rms value of phase angle. For *n = 1-6*, voltage vector called active and the rest are called zero. Active vectors can move in forward and backward direction.

Applying the active voltage vector to the inverter switches, the speed of the flux increased based on (24) and consequently δ_ψ increased so that torque reduced. By applying zero vectors, flux movement will be zero and since the rotor flux continues its movement, δ_ψ will reduce and therefore torque will increase.

As illustrated in Fig. 6, the torque and stator flux are calculated from dq components of voltage and current presented in (27) to (31). Dq components of voltage and current are calculated based on park transformation presented in (32) [47].

$$T_e = \frac{3P}{4}(\psi_{ds}^s i_{qs}^s - \psi_{qs}^s i_{ds}^s) \tag{27}$$

$$\hat{\psi}_s = \sqrt{{\psi_{ds}^s}^2 + {\psi_{qs}^s}^2} \tag{28}$$

$$\theta_e = \sin^{-1}\frac{\psi_{qs}^s}{\hat{\psi}_s} \tag{29}$$

$$\psi_{ds}^s = \int (v_{ds} - R_{ss} i_d)dt \tag{30}$$

$$\psi_{qs}^s = \int (v_q - R_{ss} i_q)dt \tag{31}$$

$$\begin{bmatrix} F_d \\ F_q \end{bmatrix} = \frac{2}{3}\begin{bmatrix} \mathrm{Cos}\,\theta & \mathrm{Cos}\,(\theta - \frac{2\pi}{3}) & \mathrm{Cos}(\theta + \frac{2\pi}{3}) \\ -\mathrm{Sin}\,\theta & -\mathrm{Sin}\,(\theta - \frac{2\pi}{3}) & -\mathrm{Sin}(\theta + \frac{2\pi}{3}) \end{bmatrix}\begin{bmatrix} F_a \\ F_b \\ F_c \end{bmatrix} \tag{32}$$

TABLE V
SWITCHING TABLE

ψ	T	S_1	S_2	S_3	S_4	S_5	S_6
1	1	V_2	V_3	V_4	V_5	V_6	V_1
	0	V_0	V_7	V_0	V_7	V_0	V_7
	-1	V_6	V_1	V_2	V_3	V_4	V_5
-1	1	V_3	V_4	V_5	V_6	V_1	V_2
	0	V_7	V_0	V_7	V_0	V_7	V_0
	-1	V_5	V_6	V_1	V_2	V_3	V_4

The switching table for vector control of inverter is presented in Table V.

APPENDIX B

Nickel- Cadmium and Nickel-Metal-Hydride batteries equations are presented in (33) and (34).

During charging mode:

$$E_{batt(\text{int})} = E_0 - \left(K\frac{Q_c}{Q_c - Q(t)}i\right) - (K)\frac{Q_c}{Q_c - Q(t)}Q(t) + Laplace^{-1}\left(\frac{Exp(s)}{\text{mode}(s)}.0\right) \tag{33}$$

During discharging mode:

$$E_{batt(\text{int})} = E_0 - \left(K\frac{Q_c}{|Q(t)|+0.1Q_c}i\right) - (K)\frac{Q_c}{Q_c - Q(t)}Q(t) + Laplace^{-1}\left(\frac{Exp(s)}{\text{mode}(s)}.\frac{1}{s}\right) \tag{34}$$

Where E_0 is the constant voltage, *K* is the Polarization constant, Q_c is the maximum capacity of battery, *i* is the low frequency current dynamic, *Exp(s)* exponential zone dynamic of voltage, mode(s) is the mode of charging (mode(s) $= 1$) and discharging (mode(s) $= 0$) of the battery.

Internal voltage of supercapacitor is also described by (35).

$$E_{SC(\text{int})} = \frac{N_s Q(t) d}{N_p N_e \varepsilon\varepsilon_0 A_i} + \frac{2N_e N_s RT}{F}\sinh^{-1}\left(\frac{Q(t)}{N_p N_e^2 A_i\sqrt{8RT\varepsilon\varepsilon_0 c}}\right) \tag{35}$$

Where, N_s, N_p are number of series and parallel capacitors, N_e is the number of electrodes layers, ε and ε_0 are permittivity of material and air, respectively. *R* and *T* are ideal gas constant and operating temperature, respectively and A_i is the interfacial area between electrodes and electrolyte.

REFERENCES

[1] A. Gonzalez-Gil, R. Palacin, and P. Batty, "Sustainable urban rail systems: Strategies and technologies for optimal management of regenerative braking energy," *Energy Convers. Manage.*, vol. 75, pp. 374–388, 2013.

[2] M. Khodaparastan, A. A. Mohamed, and W. Brandauer, "Recuperation of regenerative braking energy in electric rail transit systems," *IEEE Trans. Intell. Transp.*, to be published, doi: 10.1109/TITS.2018.2886809.

[3] N. Ghaviha, J. Campillo, M. Bohlin, and E. Dahlquist, "Review of application of energy storage devices in railway transportation," *Energy Procedia*, vol. 105, pp. 4561–4568, 2017.

[4] M. Khodaparastan and A. Mohamed, "Supercapacitors for electric rail transit system," in *Proc. 6th Int. Conf. Renewable Energy Res. Appl.*, 2017, vol. 5, pp. 1–6.

[5] A. Rupp, H. Baier, P. Mertiny, and M. Secanell, "Analysis of a flywheel energy storage system for light rail transit," *Energy*, vol. 107, pp. 625–638, 2016.

[6] C. Design, "Appendix 7 conceptual design of electrification system," 2010. [Online]. Available: http://www.gotransit.com/electrification/en/project_history/Appendix Files/Appendix 7.pdf

[7] Siemens, "System design with Sitras Sidytrac simulation of AC and DC traction power supply," 2014. [Online] Available: https://w3.siemens.com/smartgrid/global/SiteCollectionDocuments/en/rail-solutions/railway-electrification/system-design/sitras-sidytrac-en.pdf. Accessed on: Feb. 5, 2019.

[8] Railway Solutions, "eTraX rail traction systems," 2016.

[9] M. Vernon and R. A. Uher, "Program manual for the train operation model," 2016.

[10] A. Stephan, "OpenPowerNet—Simulation of railway power supply," *WIT Trans. Built Environ.*, vol. 103, pp. 449–459, 2008.

[11] J. Melorose, R. Perroy, and S. Careas, "Railroad simulation using OpenTrack," *WIT Trans. Built Environ.*, vol. 1, pp. 45–54, 2015.

[12] J. Van Mierlo and G. Maggetto, "Innovative iteration algorithm for a vehicle simulation program," *IEEE Trans. Veh. Technol.*, vol. 53, no. 2, pp. 401–412, Mar. 2004.

[13] R. A. Jabr and I. Džafić, "Solution of DC railway traction power flow systems including limited network receptivity," *IEEE Trans. Power Syst.*, vol. 33, no. 1, pp. 962–969, Jan. 2018.

[14] B. Mohamed and P. Arboleya, "Modified current injection method for power flow analysis in heavy-meshed DC railway networks with nonreversible substations," *IEEE Trans. Veh. Technol.*, vol. 66, no. 9, pp. 7688–7696, Sep. 2017.

[15] P. Arboleya, G. Diaz, and M. Coto, "Unified AC/DC power flow for traction systems: A new concept," *EEE Trans. Veh. Technol.*, vol. 61, no. 6, pp. 2421–2430, Jul. 2012.

[16] W. Liu, Q. Li, and M. Chen, "Study of the simulation of DC traction power supply system based on AC/DC unified Newton-Raphson method," in *Proc. 1st Int. Conf. Sustain. Power Gener. Supply*, 2009, pp. 1–4.

[17] D. Seimbille, "Design of power supply system in DC electrified transit railways - Influence of the high voltage network," Degree Project, KTH Roy. Inst. Technol., Stockholm, Sweden, 2014.

[18] M. A. Ríos, G. Ramos, and U. D. L. Andes, "Power system modelling for urban massive transportation systems," in *Infrastructure Design, Signalling and Security in Railway*. Rijeka, Croatia: InTech, 2012.

[19] A. Finlayson, C. J. Goodman, and R. D. White, "Investigation into the computational techniques of power system modelling for a DC railway," *WIT Trans. Built Environ.*, vol. 88, pp. 735–745, 2006.

[20] D. Yu, K. Lo, X. Wang, and X. Wang, "MRTS traction power supply system simulation using Matlab/Simulink," in *Proc. Veh. Technol. Conf.*, 2002, pp. 308–312.

[21] M. Z. Chymera, A. C. Renfrew, M. Barnes, and J. Holden, "Modeling electrified transit systems," *IEEE Trans. Veh. Technol.*, vol. 59, no. 6, pp. 2748–2756, Jul. 2010.

[22] S. Chenh, M. Sautreuil, D. Riu, and N. Retière, "Quasi-static decoupled load flow modelling of a power supply network with AC-DC converters applied to light rail system," in *Proc. IEEE Veh. Power Propulsion Conf.*, 2008, pp. 26–36.

[23] S. Park and L. Koo, "The analysis of electrified ground transportation network," *IEEE Trans. Power App. Syst.*, vol. PAS-96, no. 1, pp. 240–247, Jan. 1977.

[24] C. Mayet, P. Delarue, A. Bouscayrol, E. Chattot, and J. Verhille, "Comparison of different EMR-based models of traction power substations for energetic studies of subway lines," *IEEE Trans. Veh. Technol.*, vol. 65, no. 3, pp. 1021–1029, Mar. 2016.

[25] C. Mayet *et al.*, "Comparison of different models and simulation approaches for the energetic study of a subway," *IEEE Trans. Veh. Technol.*, vol. 63, no. 2, pp. 556–565, Feb. 2014.

[26] EMR, "Modelling and control using EMR, application to HEVs and others," 2017. [Online]. Available: http://www.emrwebsite.org, Accessed on: Jan. 5, 2019.

[27] A. Rufer, D. Hotellier, and P. Barrade, "A supercapacitor-based energy storage substation for voltage compensation in weak transportation networks," *IEEE Trans. Power Del.*, vol. 19, no. 2, pp. 629–636, Apr. 2004.

[28] T. Kovaltchouk, B. Multon, H. Ben Ahmed, J. Aubry, and P. Venet, "Enhanced aging model for supercapacitors taking into account power cycling: Application to the sizing of an energy storage system in a direct wave energy converter," *IEEE Trans. Ind. Appl.*, vol. 51, no. 3, pp. 2405–2414, May/Jun. 2015.

[29] M. Khodaparastan and A. Mohamed, "A study on supercapacitor wayside connection for energy recuperation in electric rail systems," in *Proc. IEEE Power Energy Soc. Gen. Meeting*, 2017, pp. 1–5.
[30] Z. Yang, Z. Yang, H. Xia, and F. Lin, "Brake voltage following control of supercapacitor-based energy storage systems in metro considering train operation state," *IEEE Trans. Ind. Electron.*, vol. 65, no. 8, pp. 6751–6761, Aug. 2018.
[31] H. Hayashiya *et al.*, "Proposal of a novel control method of Li-ion battery system for regenerative energy utilization in traction power supply system," in *Proc. IEEE Int. Power Electron. Motion Control Conf.*, 2016, pp. 298–303.
[32] C. H. Bae, M. S. Han, Y. K. Kim, C. Y. Choi, and S. J. Jang, "Simulation study of regenerative inverter for DC traction substation," in *Proc. Int. Conf. Electr. Mach. Syst.*, 2005, pp. 1452–1456.
[33] D. Cornic, "Efficient recovery of braking energy through a reversible dc substation," in *Proc. Int. Conf. Elect. Syst. Aircraft, Railway Ship Propulsion*, 2010, pp. 1–9.
[34] P. B. Mellitt, B. Tech, C. Eng, and Z. S. Mouneimne, "Simulation study of DC transit systems with inverting substations," *Proc. Inst. Elect. Eng. B, Electr. Power Appl.*, vol. 131, no. 2, pp. 38–50, Mar. 1984.
[35] M. Khodaparastan and A. Mohamed, "Modeling and simulation of regenerative braking energy in DC electric rail systems," in *Proc. IEEE Transp. Electrif. Conf. Expo.*, 2018, pp. 1–6.
[36] G. Zhang, J. Qian, and X. Zhang, "Application of a high-power reversible converter in a hybrid traction power supply system," *Appl. Sci.*, vol. 7, no. 3, pp. 282–301, 2017.
[37] R. Barrero, O. Hegazy, P. Lataire, T. Coosemans, and J. Van Mierlo, "An accurate multi-train simulation tool for energy recovery evaluation in DC rail networks," *Int. Rev. Model. Simul.*, vol. 4, no. 6, pp. 2985–3003, 2011.
[38] D. Iannuzzi and D. Lauria, "A new supercapacitor design methodology for light transportation systems saving," in *Energy Management System*, P. Giridhar Kini, Ed. Intech, 2011, ch. 9, pp. 183–198.
[39] R. Barrero, X. Tackoen, and J. Van Mierlo, "Quasi-static simulation method for evaluation of energy consumption in hybrid light rail vehicles," in *Proc. IEEE Veh. Power Propulsion Conf.*, 2008, pp. 1–7.
[40] P. Arboleya, "DC Railway simulation including controllable power electronic and energy storage devices," *IEEE Trans. Power Syst.*, vol. 33, no. 5, pp. 5319–5329, Sep. 2018.
[41] C. J. Goodman, "Overview of electric railway systems and the calculation of train performance," in *Proc. 9th IET Prof. Dev. Course Electr. Tract. Syst.*, 2006, pp. 13–36.
[42] D. Harris, "Central corridor light rail project design criteria (Revision 0)," Metropolitan Council, Minneapolis, MN, USA, Jul. 2008. [Online] Available: https://metrocouncil.org/Transportation/Publications-And-Resources/Transit/Central-Corridor-Light-Rail-Transit-Design-Criteri.aspx. Accessed on: Feb. 5, 2019.
[43] R. J. Gran, *Numerical Computing With Simulink*: *Creating Simulations*, vol. 1. Philadelphia, PA, USA: SIAM, 2007.
[44] G. S. Buja and M. P. Kazmierkowski, "Direct torque control of PWM inverter-fed AC motors—A survey," *IEEE Trans. Ind. Electron.*, vol. 51, no. 4, pp. 744–757, Aug. 2004.
[45] C. Lascu, I. Boldea, and F. Blaabjerg, "Direct torque control of sensorless induction motor drives: A sliding-mode approach," *IEEE Trans. Ind. Appl.*, vol. 40, no. 2, pp. 582–590, Mar./Apr. 2004.
[46] A. A. Pujol, "Direct torque control of induction motors," in *Proc. 2nd Int. Res. Edu. Colloq. Electron.*, 2001, pp. 35–38.
[47] B. K. Bose, *Modern Power Electronics and AC Drives*. Englewood Cliffs, NJ, USA: Prentice-Hall, 2001.
[48] G. E. Moglen, *Fundamentals of Power Electronics*. New York, NY, USA: Springer, 2015.
[49] New York City Transit, "Subway timetable line 7," 2018.
[50] M. Khodaparastan, O. Dutta, and A. Mohamed, "Wayside energy storage system for peak demand reduction in electric rail systems," in *Proc. IEEE Ind. Appl. Society Annu. Meeting*, 2018, pp. 1–5.

Mahdiyeh Khodaparastan received the B.Sc. and M.Sc. degrees in electrical power engineering from the Amirkabir University of Technology, Tehran, Iran, in 2010 and 2012, respectively. She is currently working toward the Ph.D. degree and is a Research Assistant with the Smart Grid Laboratory, The City College of New York, New York, NY, USA. Her research interests include energy storage systems design and development as well as power system protection and distributed generators.

Oindrilla Dutta was born in Calcutta, India. She received the B.Tech. degree from the West Bengal University of Technology, Kolkata, India, in 2014. She is currently working toward the Ph.D. degree with the Smart Grid Laboratory, Electrical Engineering Department, The City College of New York, New York, NY, USA. Her current research interests are adaptive control and stability of smart grid, renewable energy systems, interdependent networks, energy management systems, rail transportation, and power grid modeling.

Mahmoud Saleh received the M.E. degree from The City College of New York, New York, NY, USA, in 2013. He is currently working toward the Ph.D. degree with the Smart Grid Laboratory, Department of Electrical Engineering, The City College of New York. His research interest includes enhancing grid resilience, microgrids design, control, and automation, applications of complex network analysis in electric power systems, impact of ICT degradation on the smart grid, and regenerative energy braking in electric traction systems.

Ahmed A. Mohamed (El-Tallawy) (GS'09–M'13–SM'17) is an Assistant Professor of electrical engineering and the Founding Director of the Smart Grid Interdependencies Laboratory, The City University of New York, New York, NY, USA. He is also with the Department of Electrical Engineering (on leave), Menia University, Menia, Egypt. His current research interests include critical infrastructure interdependencies, smart grid resiliency, and electric transportation.